



EXPERIMENTAL INVESTIGATION OF FLUIDIC THRUST VECTORING BY SHOCK VECTOR CONTROL OF AN IDEAL CONTOUR NOZZLE

Akshay S N¹, Mullangi Kalyan², Sreeharsha S³, Yadala Sandeep Kumar⁴,
K Ramesh⁵, Ramesh M Chalkapure⁶

E-Mail Id: snakshay8@gmail.com, rameshmc.mech@bmsce.ac.in

^{1,2,3,4,5,6}Department of Mechanical Engineering, BMS College of Engineering, Bangalore, India

Abstract: The vectoring performance of shock vector control was investigated for a two-dimensional supersonic nozzle designed using the method of characteristics with injector shape being slot-shaped (rectangular). Unlike a conical nozzle, the method of characteristics nozzle has a divergence angle that varies which affects the dynamics of the flow at the exit of the nozzle. The nozzle was designed with $NPR_D = 9$ and the injector was fixed and positioned at 80% of the divergence length with the injection angle being right angles to the nozzle wall. This study is focused on the effects of mass flow ratio on shock vector control. The mass flow ratio was controlled by varying the stagnation pressure ratios. Schlieren imaging with a single mirror coincident system was used to visualize the flow field in the nozzle. Experiments were performed with air as both primary and secondary fluid for a range of primary and secondary pressures. The data obtained were compared with numerical simulations which were run using different turbulence models, with Sparlat-Allmaras one equation and standard k- ϵ model, under the same experimental conditions. The results obtained using the Sparlat-Allmaras one equation model were found to closely match with that of the experiments. On increasing the mass flow ratio, the deflection or vectoring angles were observed to be increasing but up to a certain maximum. The maximum experimental deflection angle achieved was approximately 12° and vectoring coefficient being 2.383. For flow cases where reattachment occurs, downstream of the injector, the nozzle designed using the method of characteristics can, yet, direct the flow parallel to the axis, hence producing a lesser opposing moment than in case of a conical nozzle.

Keywords: fluidic thrust vectoring, shock vector control, method of characteristics, secondary transverse injection, transverse gas injection.

1. INTRODUCTION

Thrust vectoring or thrust vector control (TVC) is a flight control technique widely used in rockets, spacecraft, and aircraft. TVC method involves deflecting the exhaust flow in such a direction that it transfers some momentum in the transverse direction generating a moment. It is used when conventional steering systems such as rudders and flaps are ineffective in environments such as outer space, at low speeds or high angle of attacks. In rockets, it is used to generate pitch and yaw moments by deflecting the thrust vector so as to be able to control the angular velocity about the center of mass, by means of a gimballed engine, hence aiding in controlling the trajectory. In spacecraft, it is used for fine attitude adjustments or modulating its velocity, examples: Vernier thruster, cold gas thrusters. In aircraft, it is used to enhance maneuverability take-off and landing performances operational examples include the AV-8B Harrier II, Lockheed Martin F-35 Lightning II, which are capable of vertical take-off and landing. Conventional thrust vectoring systems employ mechanical means, such as actuators, for thrust vectoring which are usually heavy mechanisms. Fluidic thrust vectoring consists of different techniques of manipulating the thrust vector without the use of mechanical actuators. These include the throat skewing method, co-flow and counter-flow method (based on the Coanda effect) and shock vector control (SVC). Fluidic thrust vectoring systems are cost-effective, relatively light and simpler in design compared to the mechanical means of achieving thrust vectoring. They are also shown to have faster dynamic response[1] and relatively lighter vectoring mechanisms which are some of the characteristics that are desired for propulsion systems of spacecraft and rockets, hence, have a potential application in small spacecraft and CubeSats. Fluidic thrust vectoring by the SVC method changes the direction of thrust by injecting a secondary fluid into the diverging part of a nozzle. This fluidic injection acts as an obstruction to the incoming supersonic flow, hence causing an oblique shock in the divergent section. The primary supersonic flow gets deflected on encountering the oblique shock generating momentum in the transverse direction at the expense of axial thrust. The deflection angle or the vectoring angle is greatly influenced by mass flow ratio (MFR), injector location, injector design, and secondary injection angle. The mass flow ratio can be indirectly controlled by varying the secondary pressure ratio (SPR). Another application of SVC which has been extensively investigated by is thrust modulation of solid rocket engines. In solid rocket engines, the fuel combustion rate is difficult to control which precludes the ability to vary the thrust. Thrust modulation by SVC involves using multiple symmetric injection ports that inject secondary jet inducing shocks that modulate the thrust magnitude. FTV by SVC can

also avoid or reduce the number of cold gas thrusters in spacecraft reaction control system (RCS), thus reducing the weight of spacecraft and increasing the payload capacity of the launch vehicle. This paper describes the initial experimental investigations of the performance of SVC as a thrust vectoring mechanism in a MOC nozzle.

2. EXPERIMENTAL SETUP

The thrust vectoring (by SVC) experiments were performed in the 'Energy Conversion Laboratory' of the institution. A test rig (small scale) was designed to carry out the experiments to determine the performance of fluidic thrust vectoring. A multi-stage reciprocating air compressor, in the institution laboratory, with a capacity of 350 liters provided the supersonic nozzle with high-pressure air at the nozzle inlet. The output of the multi-stage reciprocating air compressor was connected to the primary air supply circuit with a pressure regulator which ensured the safety of the system (Fig.2.1). The air supply to the inlet of the nozzle was controlled by using a solenoid valve which was operated via a NI module. A single-stage reciprocating air compressor, in the institution laboratory, was used to supply the injector with the secondary air for shock vector control. The pressure regulating valve connected to the output of the compressor (similar to that of the primary air supply circuit), enabled the secondary air supply circuit to provide the injector with different secondary pressures, which in turn varies MFR and ensured safety. The pipework and the valves used in the setup set an upper bound to the size of the nozzle throat, since, to ensure that there is choked flow in the nozzle, the region with the minimum cross-sectional area considering the whole primary air supply circuit should be at the nozzle throat.

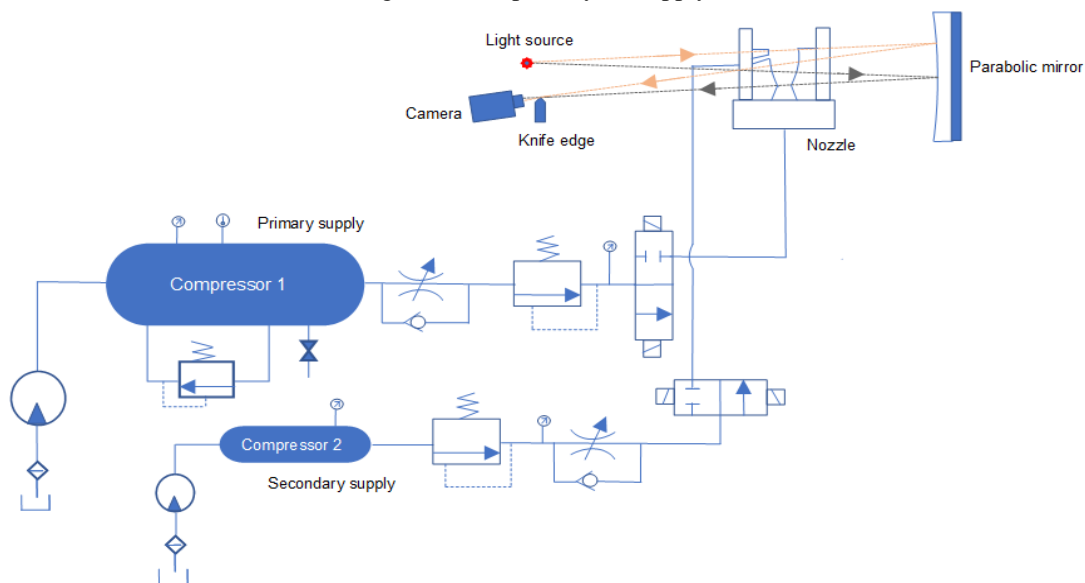


Fig. 2.1 Experimental Setup Scheme

2.1 Thrust Vectoring Nozzle Design

The thrust vectoring nozzle was designed using the method of characteristics with a rectangular cross-section. This approach was chosen since in a MOC nozzle the divergence angle varies and the flow can be made parallel to the axis of the nozzle, unlike a conical nozzle in which the flow angle is influenced by the constant and non-varying divergence angle. This characteristic can affect the net deflection (vectoring), upon secondary fluidic injection, since the injector can now be placed at the portion of the divergent section, of a MOC nozzle, where the divergence angle is the least (is lesser than that of a conical nozzle designed to achieve the same exit conditions). Hence, enabling effective thrust vectoring. In a MOC nozzle, the required exit conditions can be achieved with a shorter divergence length and the effect of the divergence angle on the net deflection of the flow can be reduced by shifting the injector location closer to the nozzle exit. The efficiency of a conical nozzle can be improved by reducing the divergence angle but would yield a larger divergence length to achieve the same exit conditions. Initial investigations were performed with a 2D nozzle design. The maximum safe pressure of the multi-stage reciprocating air compressor was 12bar, a MOC nozzle with $NPR_D = 9$ was chosen so that the performance of the nozzle can be studied with different flow regimes, i.e., over-expanded and under-expanded. The equations of the characteristics lines were determined by solving the compatibility equations, equations (1) and (2), through linear characterization, Fig.2.2 shows the contour of the divergent section of the nozzle and characteristics lines, whose coordinates were obtained by solving the compatibility equations in MatLab. It is important to ensure that divergent section provides sufficient area to position the injector, which depends on the throat diameter or width. The width of the nozzle throat was set to 11mm and based on the size of the pipework, the throat area was fixed at 11 x 5mm, providing a divergence length of 30.45mm.

$$\theta + \nu = C^- \quad (1)$$

$$\theta - \nu = C^+ \quad (2)$$

DOI Number: <https://doi.org/10.30780/IJTRS.V05.I01.004>

pg. 26

www.ijtrs.com

www.ijtrs.org

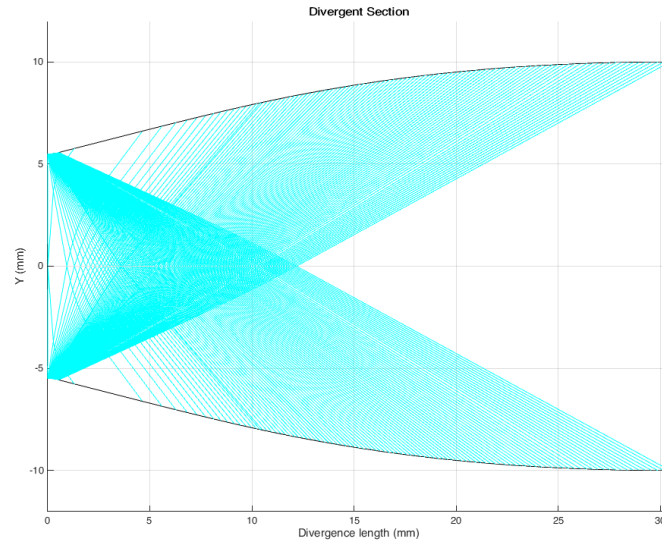


Fig. 2.2 Divergent Section Profile and the Characteristics Lines (NPR_D =9, throat width = 11mm)

A slot-shaped injector design was employed. The injector was positioned at 80% of the divergence length and perpendicular to the surface of the nozzle. The single-stage reciprocating air compressor of maximum safe pressure of 6 bar was used to provide the injector with pressurized fluid (air) for shock vector control. Some of the previous thrust vectoring investigations, as in [2], [3], [4], reported that mass flow ratios around 5-10% produced maximum deflection angles and optimal vectoring with minimal thrust losses. Based on those results and the maximum safe pressure of the secondary compressor, the width of the injector was set to 2mm, giving an overall injection area of 2x5mm which was theoretically found to produce MFRs around 5%. The nozzle block was manufactured from 6061 aluminum alloy and the sidewalls, to channel the flow, were made of acrylic glass - a transparent shatter-resistant material which enabled flow visualization through schlieren imaging technique. The source for the primary fluid was being supplied by the multi-stage air compressor mentioned previously. It was necessary to know if the experimental runtime was sufficient enough for acquiring the experimental data. The state of the gas in the compressor can be modeled as:

$$\dot{m} = \frac{dm}{dt} = \frac{V}{R} \frac{d}{dt} \left(\frac{P}{T} \right) \quad (3)$$

$$\dot{m} = \frac{P_o A_e}{a} \gamma \left(\frac{\gamma + 1}{2} \right)^{\frac{-\gamma+1}{2(\gamma-1)}} \quad (4)$$

The pressure variations in the compressor tank can be determined from equations (3) and (4). Assuming the process to be adiabatic:

$$P(t) = \left(P_o^{\frac{1-\gamma}{2\gamma}} + \left(\frac{1-\gamma}{2\gamma\sqrt{\gamma RV}} \right) \left(\frac{-\gamma f(\gamma) A_e R t}{K^{\frac{-1}{2\gamma}}} \right) \right)^{\frac{2\gamma}{1-\gamma}} \quad (5)$$

Where P_o is the absolute total pressure (in Pa) in the compressor tank and $f(\gamma) = \gamma \left(\frac{\gamma+1}{2} \right)^{\frac{-\gamma+1}{2(\gamma-1)}}$

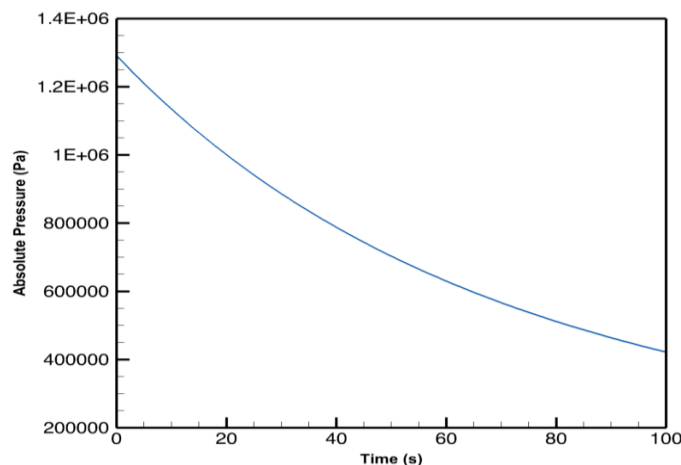


Fig. 2.3 Theoretical Pressure Variations in the Compressor Tank for an exit area of 55mm² for P_o = 13bar
DOI Number: <https://doi.org/10.30780/IJTRS.V05.I01.004> pg. 27

Fig.2.3 shows the theoretical pressure variations in the compressor tank. Hence the runtime available for an experiment, for a certain inlet primary pressure, is the time taken for the pressure in the tank to drop from the initial pressure to the required nozzle inlet pressure. The runtimes available for the range of pressures supplied by the multi-stage air compressor was found to be sufficient for recording the thrust data.

Table-2.1 Thrust Vectoring Nozzle Details

NPR _D	9
Exit mach number	2.0898
Throat area	55 mm ²
Divergent length	30.45mm
Injector location (in % of divergent length)	80%
Primary fluid	air
Secondary fluid (injection)	air

2.2 Data Acquisition System

The axial thrust and side force were measured using loadcells, the nozzle was positioned vertically on the test rig with the flow exhausting upwards. The axial thrust was measured using a pair of S-type loadcells that supported the nozzle vertically, shown in Fig.2.4(a) and Fig.2.5. A pair of support wedges transferred the load onto the S-type loadcells. Thus, the net axial force is the sum of the readings from the two s-type loadcells. The wedges created pivot points about which the nozzle could rotate. A pair of bending-type loadcells, placed on either side of the nozzle block, were used to constrain the rotation of the nozzle block, Fig.2.4(b). Hence the bending-type loadcells, in turn, measured the apparent side force and the actual side force (F_y) was determined using moment balance.

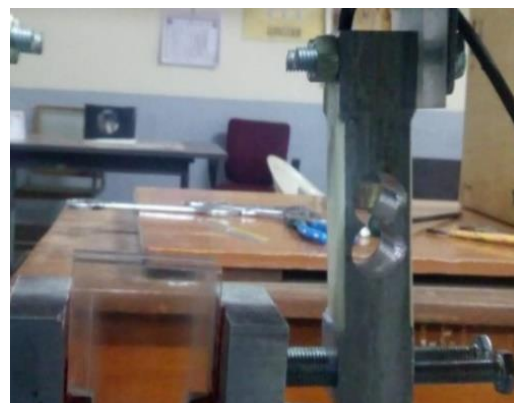
The voltage readings from the loadcells were acquired using NI 9237 module and the final force readings were recorded and processed in LabView, a graphical programming software. The data from the NI 9237 module was obtained through NI cDAQ 9188 chassis which also housed the NI 9219 module which was used to control the state of the solenoid valves. NI 9237 module has multiple input channels, each holding a load cell measurement, and is capable of acquiring fifty thousand samples per second. While having such a high sample rate, although the processing of data becomes slightly challenging, depending on the experimental run time, it helps in capturing the aberrations in the experiments. A sample rate of 25,000 was set and found to be sufficient. It is important to calibrate the load cell to ensure the accuracy of the results. One can manually add a shunt resistor, a process called shunt calibration. It is also possible to do it using LABVIEW which was found to be easier, accurate and flexible. The load cells were calibrated by using standard weights of up to 50 N. Bridge calibration was also done to remove zero error and to account for the weight of the nozzle.

2.3 Flow Visualization

A single mirror coincident schlieren imaging system was used to visualize the flow in the divergent section of the nozzle. Nikon D3100 camera with a Nikkor 55-300mm ED VR lens was used to capture the schlieren images. A parabolic mirror of diameter 250 mm and a focal length of 1400mm was used and the mirror front was coated with $Al-SiO_2$. The Mirror was tilted slightly about the vertical axis to capture the flow field in the divergent section. The tilt angle of the mirror was carefully considered so that it doesn't lead to astigmatism aberrations which causes multiple converging focal points and a knife-edge was used to manipulate the cut-off ratio. Due to the sealant that was used between acrylic sheets and nozzle flaps, the nozzle contour appears slightly distorted in the schlieren images.



(a)



(b)

Fig. 2.4 (a) S-type Loadcell, for Axial Thrust (b) Bending type Loadcell, for Side Force

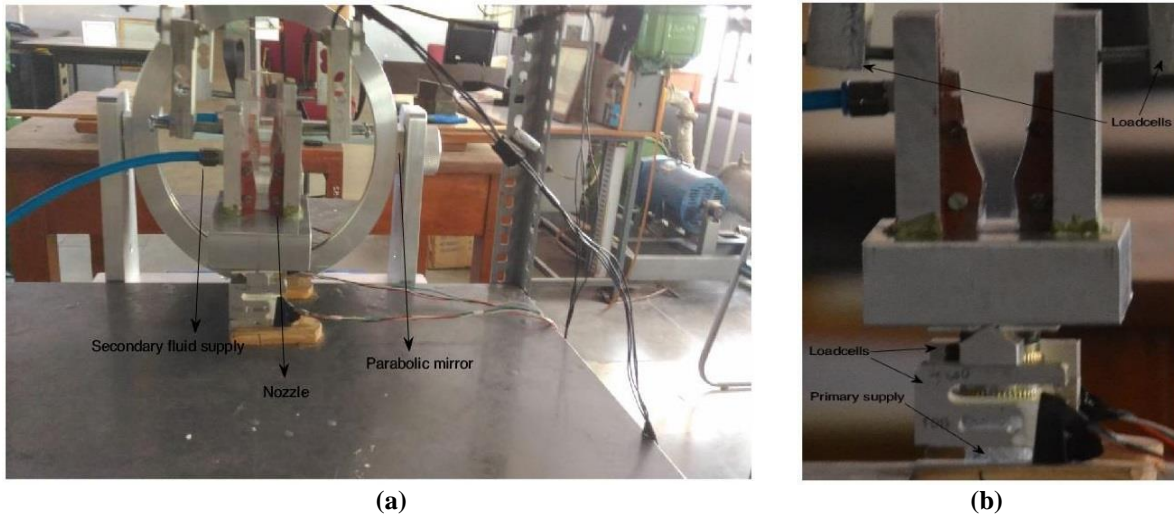


Fig. 2.5 (a) Test Setup Showing the Nozzle Block and Mirror Placement (b) Nozzle Block with Loadcell Placement and Fluidic Supplies

3. NUMERICAL METHOD

Flow simulations were conducted using the commercial software package - FLUENT. CFD numerical simulations have been extensively used to study the physics of subsonic and sonic fluidic injections into supersonic streams with various turbulence models. Simulations were performed for flow cases with total primary pressure P_p of 4bar and 5bar ($NPR = 5.376$ and $NPR = 6.471$ respectively). Previous computational studies, in [3] and [5], have investigated the Spalart-Allmaras one equation model and found that it provided stable results. Based on those investigations and due to the simplicity of the model, the Spalart-Allmaras one equation turbulence model was chosen. Since the flow physics is involved near the regions where the flow interacts with the injection-induced oblique shock, and due to the wake formations at the injector port and downstream of the oblique shock, the flow was modeled using second-order discretization scheme. Simulations of flow cases with $P_p = 4$ bar were run with Spalart-Allmaras one equation model. Other SVC studies have used $k-\epsilon$ turbulence model, a model well suited for wide range of wall-bounded and free shear flows and has been extensively used to investigate fluidic injections at various regimes, and found to be quite favorable and shown to creditably predict the physics of the flow [4], [6], [7]. Simulations of flow cases with the total inlet pressure of 5bar ($NPR = 6.471$) were run with the standard $k-\epsilon$ turbulence model and the results from chosen turbulence models were compared with corresponding experimental cases. The flow was modeled as 2D since the nozzle design has a rectangular cross-section and dry air was modeled as an ideal gas. The CFD domain used is illustrated in Fig.3.1. The designed MOC nozzle has a convergent section length of 20mm, throat diameter and converging-inlet diameter of 11mm and 15.5mm respectively and divergence length of 30.45mm. The injector was designed as slot-shaped with a width of 2mm and positioned at 80% of the divergence length. The secondary flow is injected through this slot in the upper wall of the divergent section as shown in Fig.3.1.

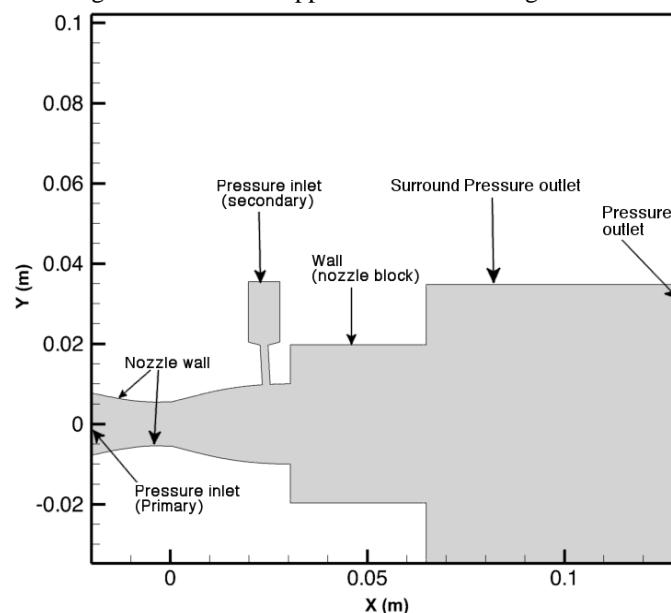


Fig. 3.1 CFD Domain Details

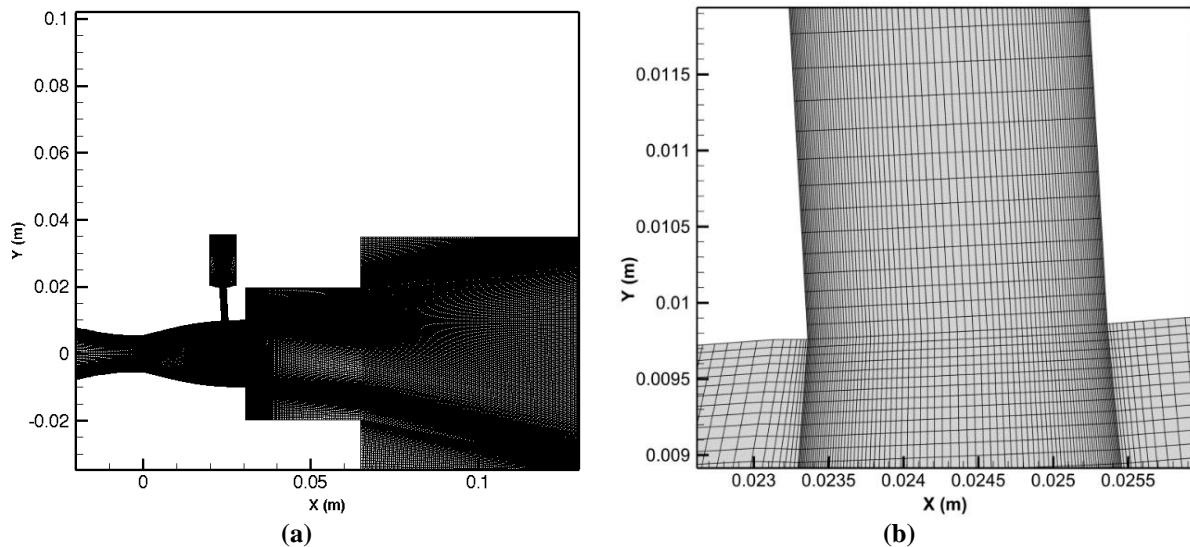


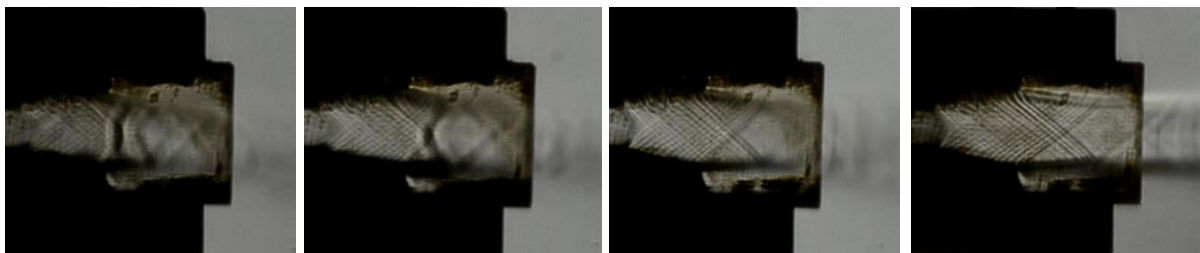
Fig. 3.2 (a) Domain mesh configuration (b) Injector-nozzle wall interface mesh configuration

Simulations of the flow in the nozzle for both the cases, with the injector and without the injector, were carried out using ANSYS Fluent software package. For the model to accurately predict the flow and capture shock interactions and viscous boundary layer effects, the grid density was increased at the wall boundaries resulting in a structured mesh of 129700 elements. The grid is denser and clustered near the throat, towards the injection region and at the injector port with the first small grid being 0.01mm increasing for up to 50 divisions with a maximum of 0.3mm, at the throat region. Reasonable convergence was obtained. The experimental schlieren image of the flow field obtained for flow case NPR = 6.471, SPR = 0.492 and the numerical schlieren, as density contours, obtained for the same flow case are shown in Fig.4.10.

4. RESULTS

4.1 Flow visualization

Useful visual data were obtained using the schlieren flow visualization technique that was employed. Initial experiments were conducted for unvectorized cases, $P_j = 0$ bar, Fig.4.1, to visualize the effects of the injector in the divergent section of the nozzle. Overexpansion of the nozzle and a slight asymmetry, with respect to the axis, in the flow was observed which was significant for the experimental case NPR = 5.376. The presence of the injector in the divergent section affected the oncoming supersonic flow inducing a weak oblique and deflecting the flow slightly.



(a) NPR = 5.376

(b) NPR = 6.471

(c) NPR = 7.565

(d) NPR = 8.659

Fig. 4.1 Experimental Schlieren for $P_j = 0$ bar

The schlieren images (Fig.4.2, 4.3, 4.4 and 4.5) obtained shows the flow pattern in the nozzle and the shock induced by the secondary fluidic injection, injection being perpendicular to the nozzle wall, for various MFR. Over-expansion of the nozzle was observed and the images also revealed the flow deflections caused due to the interactions with the oblique shocks, for various MFRs which was varied by changing the injection stagnation pressure (P_j). An oblique shock originating upstream of the injector port was observed namely, separation shock, which is governed by the PUV region, as stated in [4] and [8], and downstream of the flow, the oblique shock induced by the secondary transverse injection was observed which is the main source of primary flow deflection. For increasing MFRs, or secondary injection pressure P_j , the flow deflection and the shock angles were observed to be increasing for a fixed NPR, similar nature was observed as stated by previous studies. Fig.4.2(f) shows the flow field and the shock (bow shock) that propagates and reaches the opposite nozzle wall, while for experimental cases NPR = 6.471, 7.565, 8.569 the separation shock and the oblique shock were observed to leave the nozzle without impacting the opposite wall.

DOI Number: <https://doi.org/10.30780/IJTRS.V05.I01.004>

pg. 30

www.ijtrs.com

www.ijtrs.org

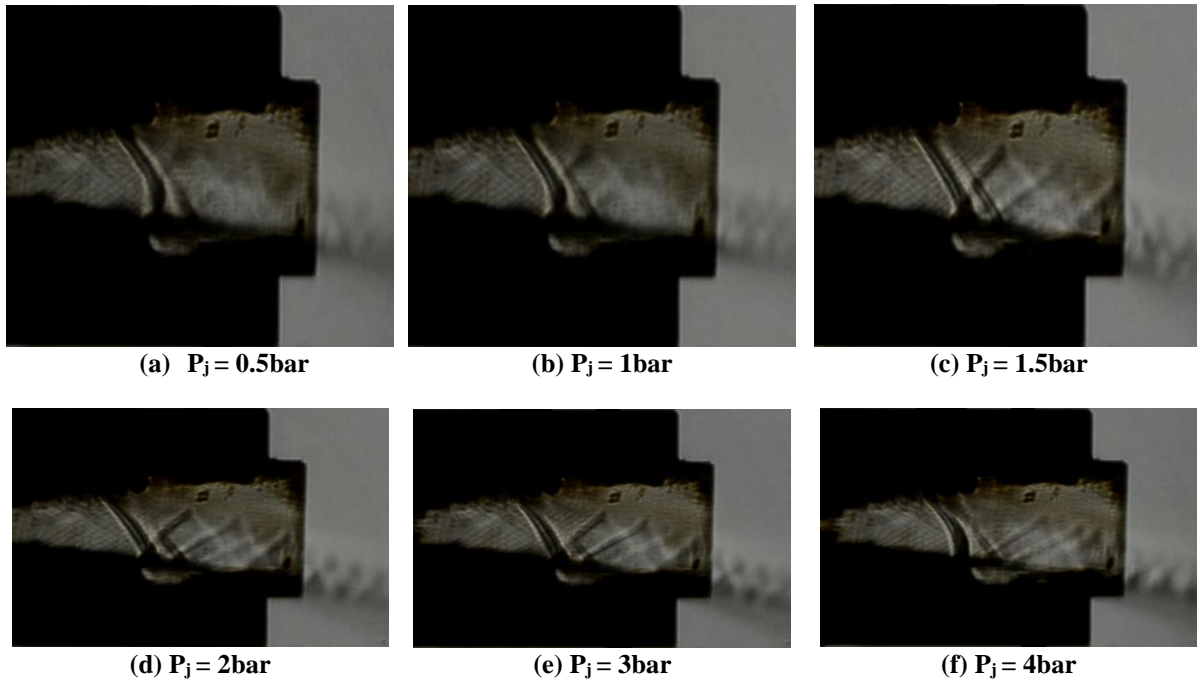


Fig.4.2 Experimental schlieren for NPR = 5.376

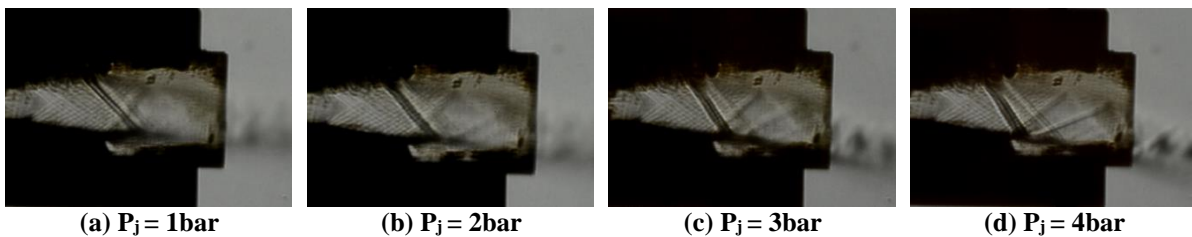


Fig.4.3 Experimental schlieren for NPR = 6.471

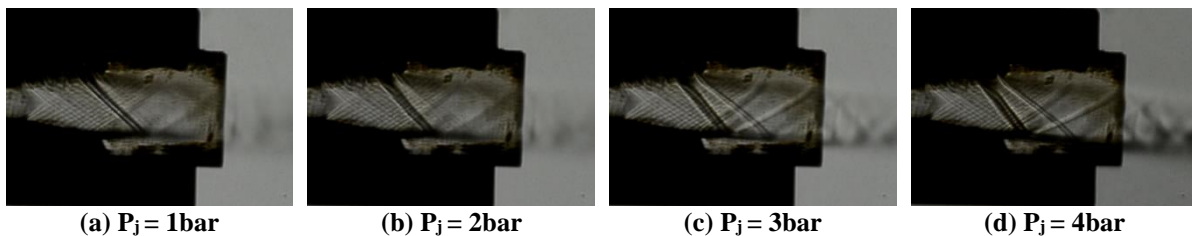


Fig.4.4 Experimental schlieren for NPR = 7.565

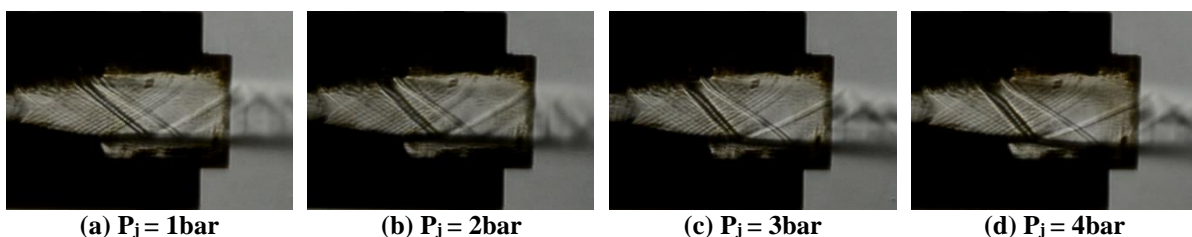


Fig. 4.5 Experimental schlieren for NPR = 8.659

4.2 Experimental thrust data

Initial experiments with the nozzle were performed without the secondary fluidic injection. This condition is different from that of a nozzle without the injection port as the injector port, although there is no secondary flow, induces shock in the divergent section. The axial thrust force was recorded and compared with the analytical value of the thrust of the same nozzle without the secondary port. Mass flow rates used in determining the thrust were not measured in the experiments directly, they were determined analytically assuming isentropic expansion process. However, the flow itself is not perfectly isentropic due to the injector induced shock in the divergent section and other slight asymmetries produced during the manufacturing of the nozzle. Hence, deviation in the thrust values, Fig.4.8(a), was observed. The nozzle was subjected to primary flow only and the thrust data was recorded. The table below, Table-4.1, summarizes the thrust data obtained for different NPR:

Table 4.1 Experimental Thrust Data for $P_j = 0\text{bar}$

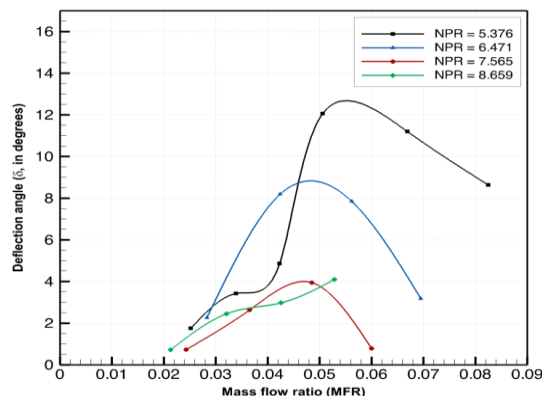
Inlet Stagnation Pressure (in bar, gauge)	NPR	Experimental Thrust (N)	Numerical Simulation Thrust (N)	Analytical Thrust (N)
4	5.376	16.157	29.155	31.408
5	6.471	25.793	36.919	38.822
6	7.565	31.438	44.739	46.237
7	8.659	40.682	52.538	53.652

Thrust vectoring capabilities of the nozzle were studied with secondary fluidic injection with total pressure ranging from 0.5 to 4bar (gauge pressure) for primary inlet total pressure of 4bar (gauge pressure) and 1bar to 4bar for primary inlet pressures of 5bar to 7bar. The injector was located at 80% of the divergence length and the secondary fluid (air) was injected at right angles to the nozzle wall. The thrust vectoring coefficient or the vector coefficient (C_v), defined in equation (6), describes the vectoring rate with respect to the amount of fluid used (air, in present investigations) for vectoring. The table below, Table-4.2, summarizes the thrust data of the thrust vectoring nozzle obtained for different NPR and mass flow ratios:

$$C_v = \frac{\tan^{-1}\left(\frac{F_y}{F_x}\right)}{MRF(100)} \quad (6)$$

Table-4.2 Experimental Thrust Data and Deflection for Various MFR

NPR	Secondary pressure P_j (bar)	SPR	MFR	Axial thrust F_x (N)	Side force F_y (N)	δ	C_v
5.376	0.5	0.287	0.0252	15.496	0.474	1.753	0.696
	1	0.389	0.0339	15.573	0.931	3.421	1.009
	1.5	0.491	0.0423	16.921	1.438	4.858	1.148
	2	0.592	0.0506	15.539	3.319	12.057	2.383
	3	0.796	0.0669	17.129	3.392	11.201	1.674
	4	1	0.0825	18.218	2.765	8.630	1.046
6.471	1	0.323	0.0283	26.162	1.031	2.257	0.798
	2	0.492	0.0424	25.188	3.624	8.187	1.931
	3	0.661	0.0562	26.205	3.611	7.846	1.396
	4	0.831	0.0695	23.277	1.291	3.175	0.457
7.565	1	0.276	0.0243	34.103	0.436	0.732	0.301
	2	0.421	0.0365	36.850	1.692	2.629	0.720
	3	0.566	0.0485	33.432	2.305	3.944	0.813
	4	0.711	0.06	31.344	0.433	0.791	0.132
8.659	1	0.241	0.0213	40.509	0.509	0.719	0.338
	2	0.368	0.0321	39.521	1.690	2.449	0.763
	3	0.494	0.0426	39.111	2.033	2.976	0.699
	4	0.621	0.0529	40.619	2.913	4.102	0.775

**Fig. 4.6 Performance of MOC Nozzle for a Range of Mass Flow Rates**

The mass flow ratio was controlled and varied by changing the secondary total pressure (P_j), which in turn varied the SPR. Fig.4.6 shows the deflection angle of the thrust vectoring angle produced for a range of mass flow ratio. The maximum deflection angle obtained was 12.057° for mass flow ratio of about 5.06%. Also, the maximum deflection achieved for different primary pressures was found to be decreasing with increase in NPR.

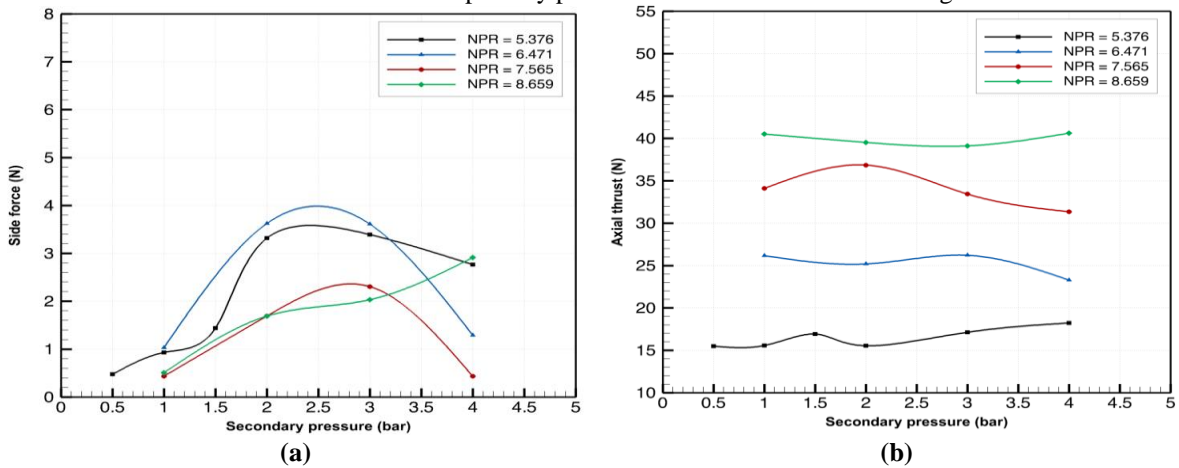


Fig. 4.7 Variation of Forces for a Range Secondary Pressure

4.3 Numerical Simulations and Analysis

Initial numerical simulations were done to validate the performance of the nozzle for different NPRs without the secondary fluidic injector. Fig.4.8(a) shows the axial thrust data extracted from numerical simulations and was found to closely match with the analytical thrust that was calculated using the predicted mass flow rate.

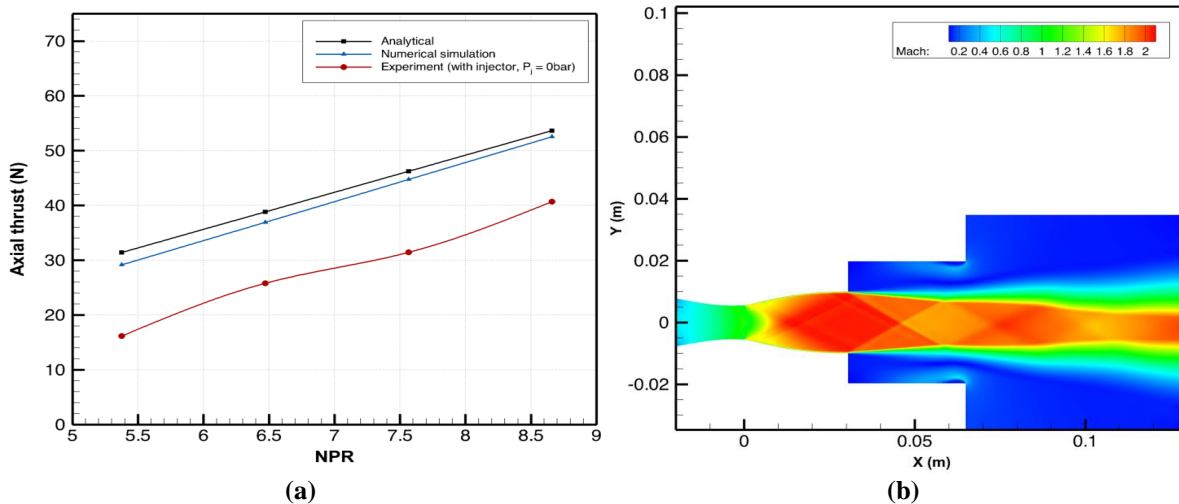


Fig. 4.8 (a) Axial thrust for different nozzle NPR (b) Mach number contour for NPR = 6.471

Simulations of the thrust vectoring nozzle were performed for NPR = 6.47 (using $k-\epsilon$ model) and NPR = 5.37 (using Sparallt-Allmaras one equation model). The injector was positioned at 80.0% of the divergent section length with the secondary fluid being injected at right angles to the wall.

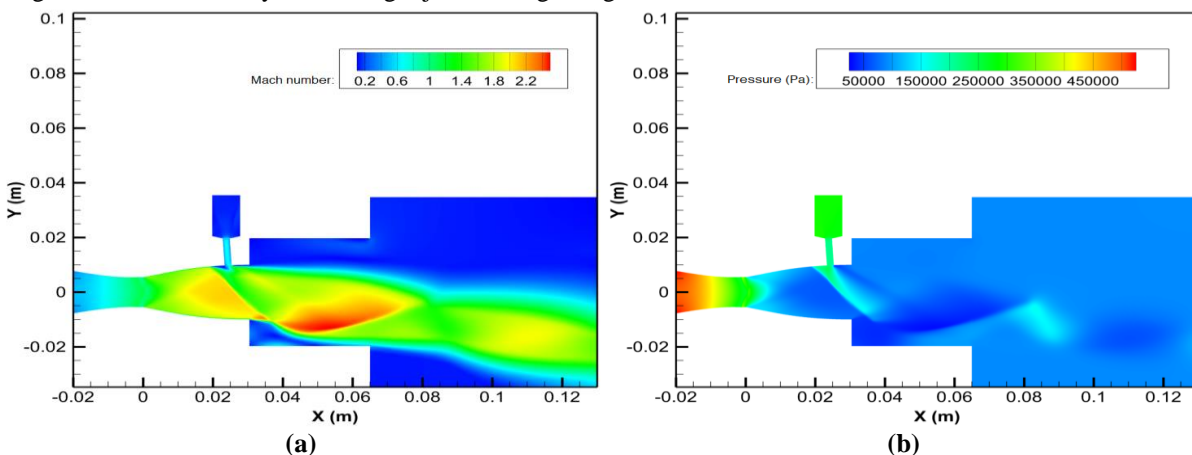


Fig. 4.9 (a) Mach Number Contour (b) Static Pressure Contour, for NPR = 6.471 SPR=0.492

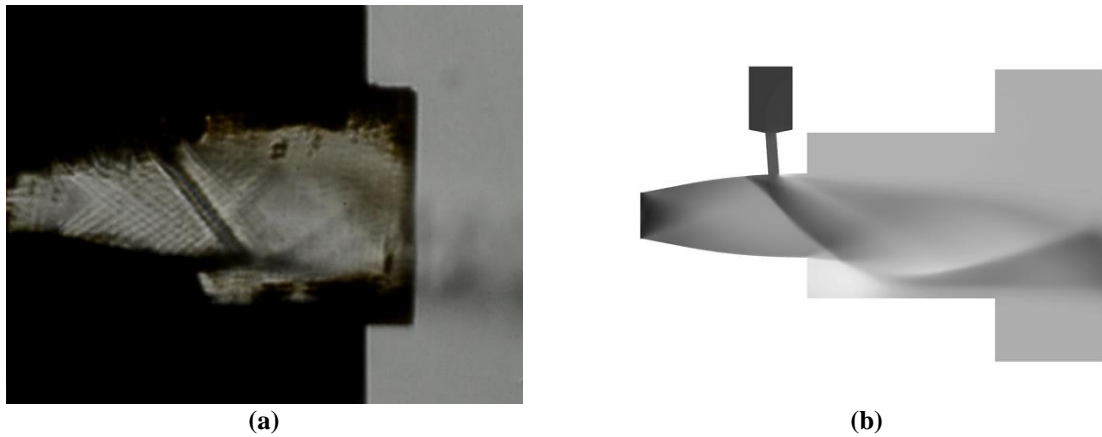


Fig. 4.10 (a) Experimental Schlieren (b) Numerical Schlieren, for NPR = 6.471 SPR=0.492

Fig.4.10(a) and 4.10(b) show experimental and numerical schlieren images obtained for NPR = 6.471 and SPR = 0.492. Variations in flow properties along the nozzle wall and at the exit were extracted from the simulations and are shown in Fig.4.11, 4.12, 4.13 and 4.14. Fig.4.11(a) shows the asymmetry in the wall shear at the nozzle walls due to pressure variations upon secondary fluidic injection. Wall pressure profiles obtained, shown in Fig.4.11(b), depicts the pressure rise upstream of the injection port due to the separation shock and vortex regions known as the primary upstream vortex (PUV) and secondary upstream vortex (SUV), and also at downstream of the injector due to another vortex region, known as primary downstream vortex (PDV), and wake formations [8]. All the regions as stated by [8] are not quite distinguishable probably due to the injector location, i.e. proximity to the nozzle exit, or they have not captured itself in the given span of iterations for the turbulence model that was used. Numerical thrust, flow deflection or the vectoring angle and other quantities were calculated from the obtained numerical data. The net axial momentum thrust was obtained by integrating the product of local density and square of the axial component of the velocity, for small y-intervals, across the exit of the nozzle. The pressure thrust was calculated by integrating the product of the pressure differential term, local $P_e - P_a$ for small y-intervals, and the area across the exit of the nozzle. Similarly, the net normal momentum thrust was calculated.

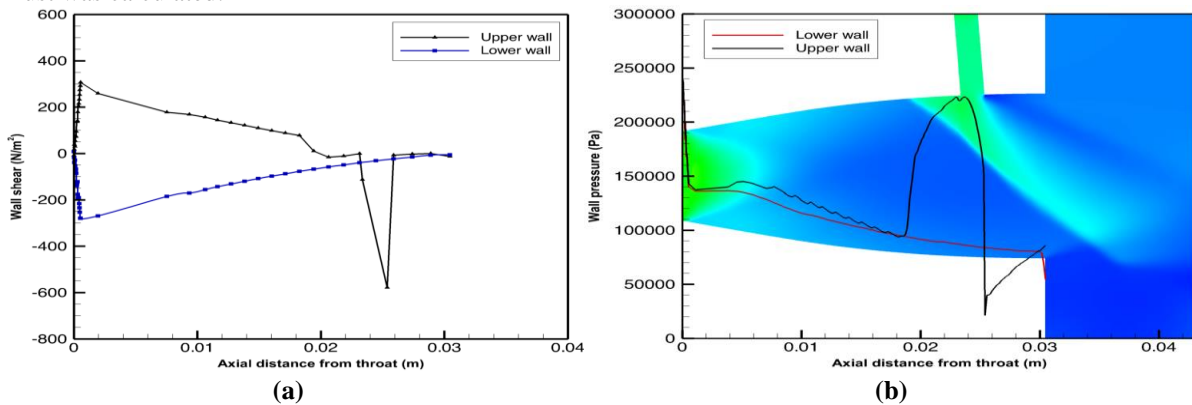


Fig.4.11 (a) Wall shear distribution (b) Wall pressure distribution, NPR = 6.471, SPR = 0.492

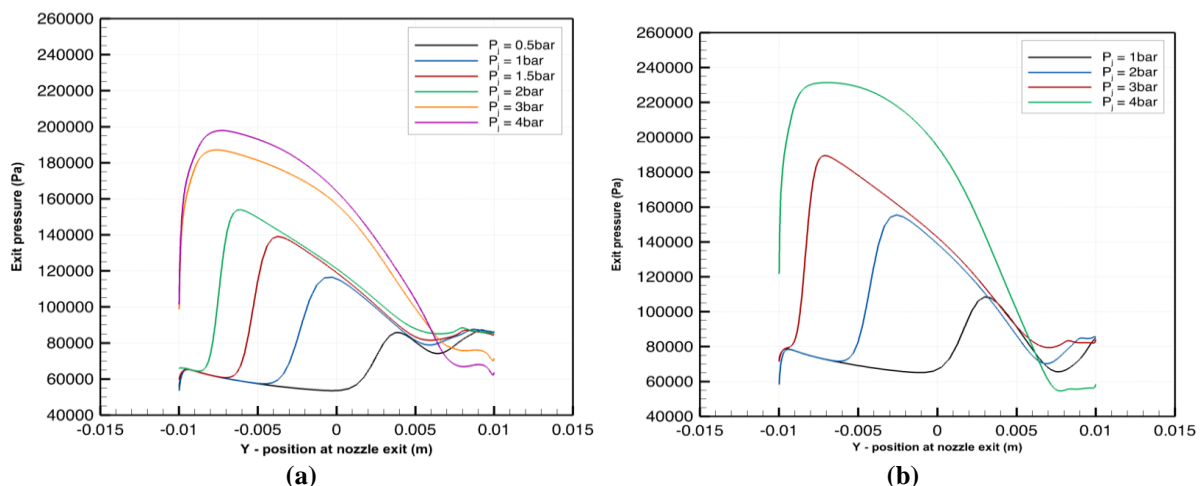


Fig. 4.12 Pressure Variations at Nozzle Exit: (a) NPR = 5.376 (b) NPR=6.471

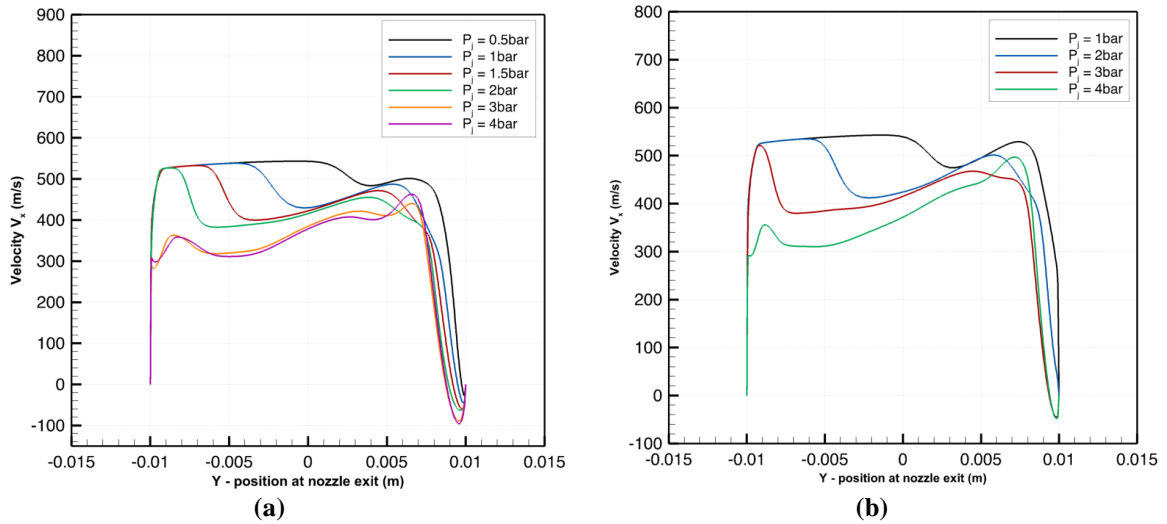


Fig.4.13 Velocity V_x at Nozzle Exit: (a) NPR = 5.376 (b) NPR = 6.471

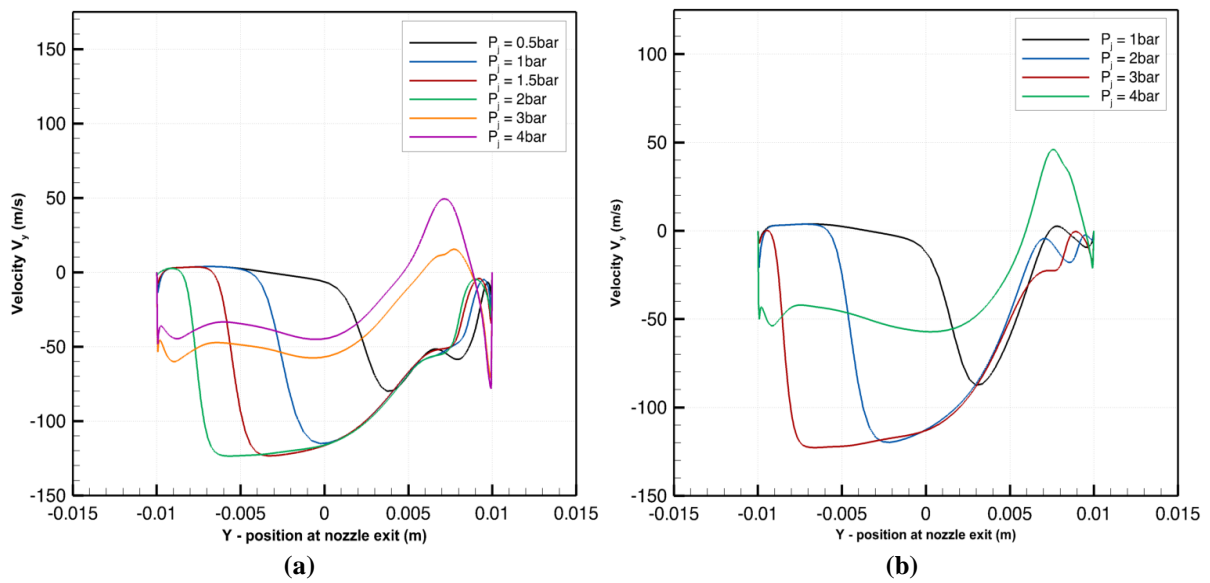


Fig.4.14 Velocity V_y at Nozzle Exit: (a) NPR = 5.376 (b) NPR = 6.471

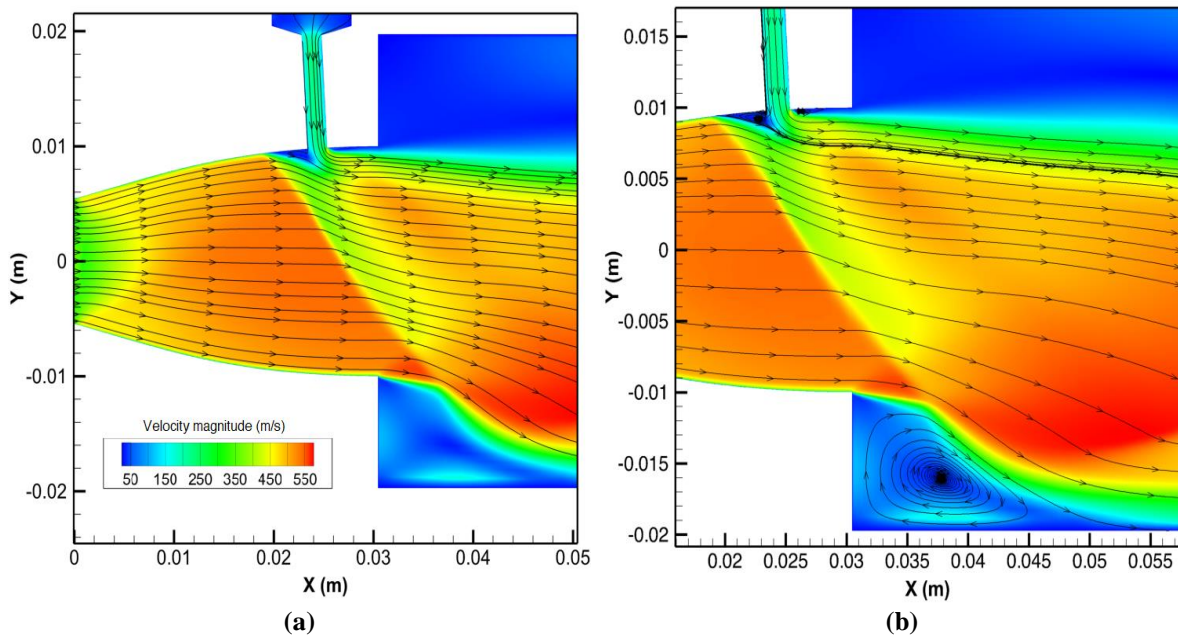


Fig. 4.15 Streamlines in the Divergent Section of the Nozzle, NPR = 6.471 SPR = 0.492, (b) Stream Traces of Vortex Regions near the Nozzle Block Wall

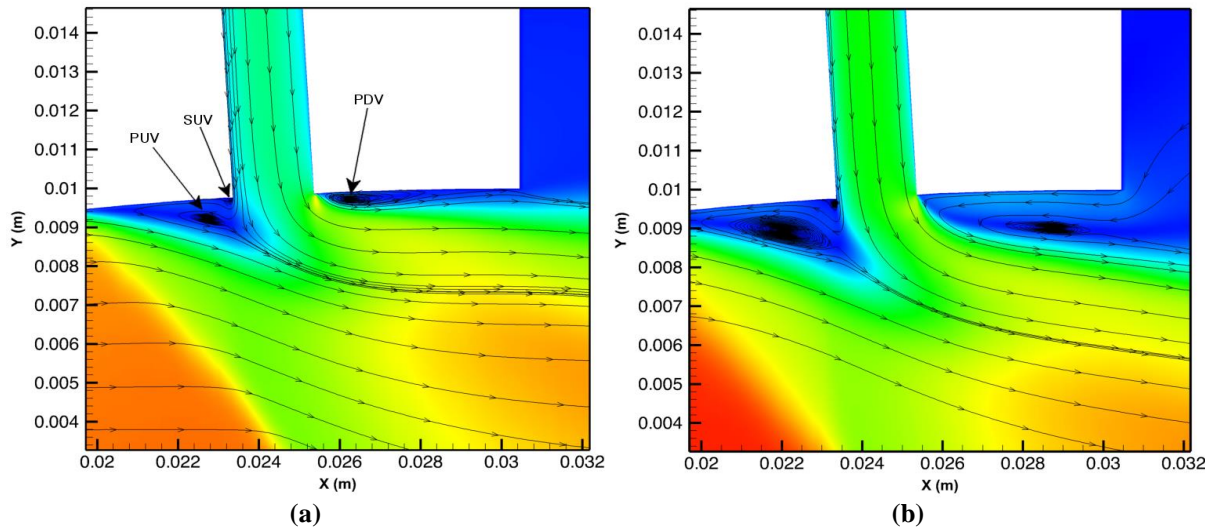


Fig. 4.16 Stream Traces Showing the Vortex Regions: (a) NPR=5.371 MFR=0.0506 (b) NPR=6.471 MFR=0.0424

Fig.4.15(a) and 4.16(a) shows the streamlines in the divergent section of the nozzle and the onset of reattachment of the flow, respectively, the flow near the upper wall at the exit is observed to be slightly directed towards the axis, due to the deflection, which is also evident from the negative velocities at the right of zero in Fig.4.14(b). In the case of conical nozzles, as observed in [3], the flow at the exit near the upper wall is seen to be directed away from the nozzle axis after reattachment. Although the NPRD of the nozzles, MFR and injector locations are different and other parameters can't be directly compared with [3], it provides useful qualitative information, discussed later, about the influence of the nozzle design on nature of flow pattern at the exit. Fig.4.16(a) shows the stream traces near the regions upstream and downstream of the injector corresponding to vortex regions PUV, SUV and PDV, for the experimental cases NPR = 5.376 and NPR = 6.471 for $P_j = 2$ bar, which are distinguishable. Fig.4.16(a) also shows the onset of the flow reattachment with the upper wall due to the formation of downstream vortices and in Fig.4.16(b) there is no appreciable reattachment of the main flow with the nozzle wall.

5. DISCUSSION AND ANALYSIS

A significant loss in axial thrust was observed when compared to the numerical and analytical results of a nozzle without the injector. Fig.4.8(a) shows the axial thrust obtained for different inlet stagnation pressures. The reduction in the thrust values, from analytical and numerical results, was due to the oblique shock induced by the injector even when there was no secondary transverse fluidic injection. However, the oblique shock-induced may not be the only factor, the pipework and the transition of different flow cross-sections, i.e., from that pipework to the rectangular nozzle inlet, pressure losses in the supply circuit causing inaccurate inlet stagnation pressure readings and differences in the actual and predicted mass flow rates also contribute to the losses. Fig.4.6 shows the variations in deflections angle for different MFR. The deflection was found to peak around 0.05 or 5% for inlet stagnation pressures 4bar, 5bar, and 6bar. However, for 7bar the same cannot be inferred due to lack of more experimental data at intermediate primary and secondary pressures. A finer experimental data acquisition was not possible due to some uncertainties in gauge readings and actual pressure. For experimental cases NPR = 7.565, 8.659 and $P_j = 4$ bar, there were slight vibrations were observed in the test rig, due to its design, which hampered the bending type loadcells from reading the actual side force that resulted in deflections angles which didn't corroborate with the numerical results, as seen in Fig.5.2(a), and visual schlieren data. Fig.4.15(b) shows vortex regions between the exhaust and lower wall of the nozzle block. This flow interaction with the type of nozzle-block wall design used was probably one of the reasons for the aberrations caused in the side force data acquisition mentioned earlier.

The MFRs corresponding to the maximum deflections, for different NPR cases, was around 0.05 or 5% which is in the range reported by other previous thrust vectoring investigations [2], [3], and [4]. However, the range of MFR corresponding to maximum deflection can be further investigated since it is also influenced by the injector location and injection angle. For increasing MFRs, or secondary injection pressure P_j , for a fixed NPR, the flow deflection and the shock angles were observed to be increasing. The maximum deflection achieved was found to be decreasing with an increase in the inlet stagnation pressure P_p , Fig.4.6, and as observed in other thrust vectoring studies, vectoring was found to be more effective for overexpanded flow. The flow deflection or the vectoring angle is known to peak when the oblique shocks encounter the opposite nozzle wall, as observed in Fig.4.2(f), and is known to generate secondary shocks that deflect the flow back towards the nozzle axis.

Previous thrust vectoring studies, in [4], have shown that the location of the injector plays an important role in shock vector control. Placing the injector further downstream reduces the distance between the injector slot and

the nozzle exit, this can help prevent the flow reattachment with the nozzle wall improving vectoring efficiency and higher vectoring angles can be achieved since the separation shock and the oblique shock would now originate further downstream preventing the impact with the opposite wall. However, vectoring can be improved even for cases where reattachment occurs. In case of a nozzle designed using the MOC, the flow dynamics at the exit are affected in a different way compared to conical nozzles since the divergence angle is not constant and, also due to the fact that nozzle wall angle at the exit can be made equal to 0° , the V_y component of the velocity at the exit near the upper wall, should ideally be zero when reattachment occurs. Fig.4.14(a) and 4.14(b) shows V_y velocity plots obtained from numerical simulations at the exit for different injection pressures, the velocity is nearly zero at the upper wall (i.e., at $y = 0.01\text{m}$), however, a spike was observed for high injection pressures (or SPR) which is probably due to the recirculation zones downstream of the injector. Hence, for cases where reattachment occurs, the flow at the nozzle exit near the upper wall can be made parallel to the axis unlike a conical nozzle where the divergence angle is fixed. Therefore, this property of the nozzle is advantageous when the injector is positioned nearer to the throat, a nozzle designed using the MOC would have a lesser opposing momentum due to the V_y component of the velocity, at the exit, than that in a conical nozzle.

Fig.5.1(a) shows the deflection angles obtained from the CFD simulations using different turbulence models. Sparlat-Allmaras one equation turbulence model used for flow cases of $\text{NPR} = 5.376$ was found to capture the flow nature similar to the experimental cases more accurately than the $k-\epsilon$ turbulence model which was used for flow cases of $\text{NPR}=6.471$. The nature of variations in the side force was also captured well by the Sparlat-Allmaras model as seen in Fig.5.2(a). As observed in experimental flow cases, the numerical deflection angle peaked when $\text{MFR} = 0.592$ for $\text{NPR} = 5.376$ and $\text{MFR} = 0.566$ for $\text{NPR} = 6.471$. However, the maximum deflection angle determined for $\text{NPR} 6.471$ was found to be greater than that of $\text{NPR} = 5.376$, this was probably due to the wall function used and the inadequate hardware resources required for the complex and computationally demanding $k-\epsilon$ turbulence model. Fig.5.1(b) shows the variations in thrust produced for different flow cases. Although, the net axial thrust determined from CFD simulations was increasing, the momentum thrust was found to be decreasing which probably is due to the increase in pressure momentum thrust upon secondary transverse injection and additional mass flow. These variations in different thrust components upon secondary transverse injection are under further investigation.

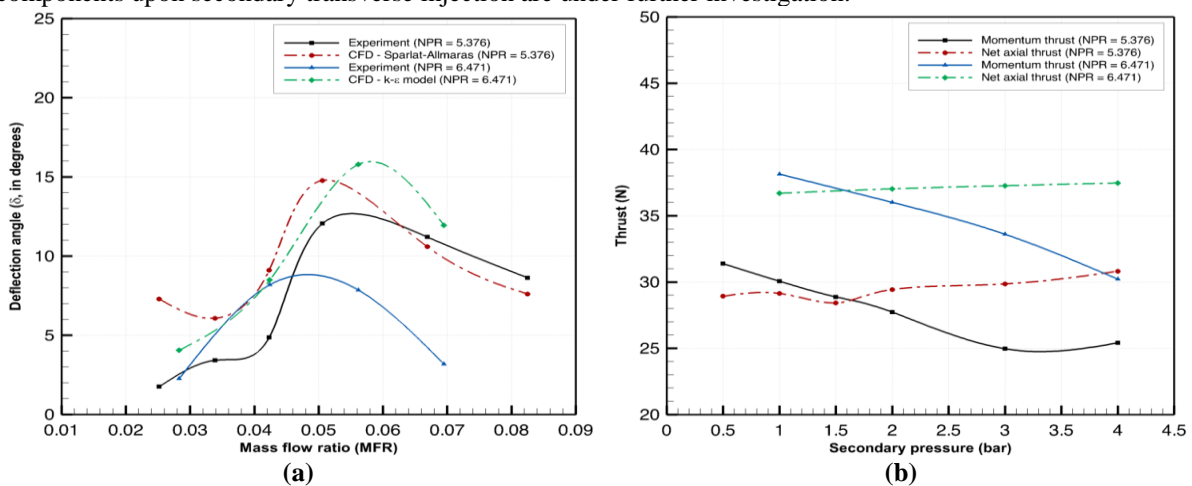


Fig. 5.1 (a) CFD-Deflections Obtained for a Range of MFR (b) Total and Momentum Thrust Variations for a Range of Secondary Pressures

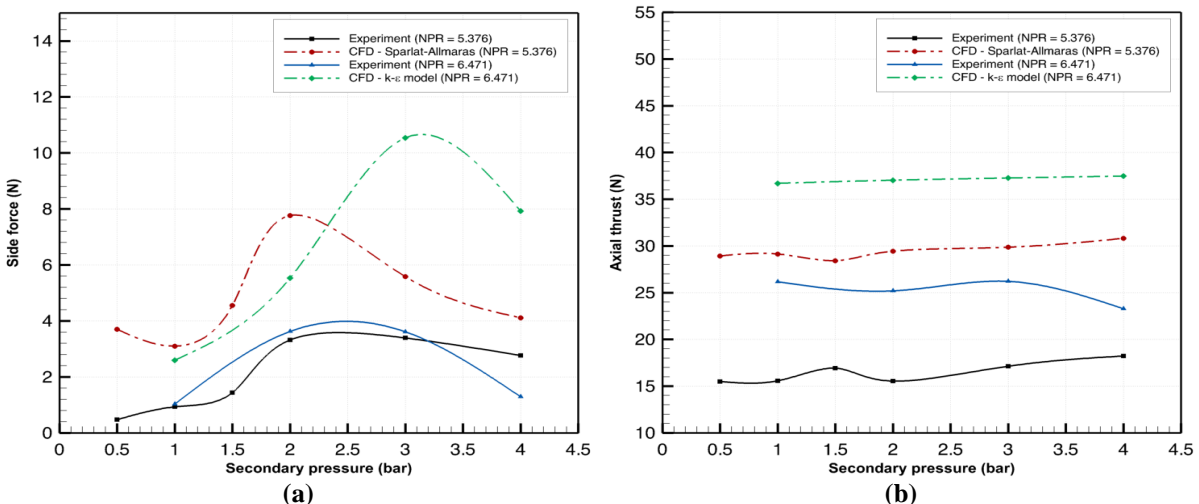


Fig. 5.2 Experimental and CFD Results of Side and Axial Thrust Force for Different Secondary Pressures
DOI Number: <https://doi.org/10.30780/IJTRS.V05.I01.004>

CONCLUSION

Fluidic thrust vector control by shock vector control is greatly influenced by various factors such as MFR, injector slot design, injection angle and position of the injector port. A 2D (rectangular cross-section) converging-diverging nozzle was designed using the method of characteristics, with a slot-shaped injector, to investigate its vectoring capabilities by varying the MFR in the nozzle. A test rig was designed to conduct the experimental investigations and a single mirror coincident schlieren system was used to visualize the flow. Experiments were performed to study the effects of MFR on shock vector control with a fixed injector positioned at 80% of the divergence length and secondary fluidic injection being 90° to the wall contour. The numerical simulations performed using Sparlat-Allmaras one equation model were able to capture the nature of variations in side-forces but the simulations with k- ϵ turbulence model over-predicted the magnitude of the side force and the possible deflection angle for few cases. However, the losses in the supply circuit leading to deviations in total pressure calculations from the experiment and vibration of the test rig that was observed could be the possible reasons for the differences in numerical and experimental results. Also, the flow simulations and analysis were two dimensional whereas the actual nozzle is three-dimensional designed to approximate a 2D flow, hence there are three-dimensional losses that can arise due to slight asymmetry in the nozzle.

Experiments were performed for a range of NPR and secondary pressures. On increasing the mass flow ratio, the shock angle and vectoring, or the deflection angle, was observed to increase but reached a maximum when the oblique shock encountered the opposite wall. This was observed in the experimental case with NPR = 5.376 and MFR = 0.0825. Therefore, to avoid the effect of the oblique shock impinging the opposite wall, placing the injector further downstream or changing the injection angle such that earlier flow separation occurs [4], can alleviate the phenomenon and provide better efficiency. The thrust vectoring achieved for flow cases with NPR = 6.471, MFR = 0.0562 and 0.0695 experimentally didn't comply with the numerical results, possible reasons mentioned previously. For the case with NPR = 5.376 and MFR = 0.0506, the experimentally determined deflection angle was found to be 12.057° , with vector coefficient $C_v = 2.383$, which the maximum that was obtained in this investigation. This can be further improved by reducing the losses and optimizing the injector design. For flow cases where reattachment occurs, a nozzle designed using MOC has a lesser opposing moment at the exit, caused by V_y component, than that of a conical nozzle which has a constant divergence angle. Injector slot design and position can also influence the SVC performance, shown by previous studies, hence optimization of the design has to be performed, depending on the nozzle design, to achieve efficient vector control of nozzle thrust. The functioning and vectoring capabilities of using SVC with different injector designs and in axisymmetric MOC nozzle are under investigation.

APPENDIX

Symbol	Description
P_p	Total pressure supplied to the nozzle (bar), gauge
P_j	Total pressure supplied to the fluidic injector (bar), gauge
P_a	Atmospheric pressure (bar)
P_o	Absolute total pressure supplied to the nozzle (Pa)
P_e	Nozzle exit pressure
NPR_D	Designed nozzle pressure ratio
\dot{m}_p	Mass flow rate of primary fluidic supply
\dot{m}_j	Mass flow rate of secondary fluidic jet
A	Speed of sound
K	Adiabatic constant
NPR	Nozzle pressure ratio
SPR	Secondary pressure ratio $\left(\frac{P_p+P_a}{P_j+P_a}\right)$
MFR	Mass flow ratio $\left(\frac{\dot{m}_j}{\dot{m}_j+\dot{m}_p}\right)$
MOC	Method of characteristics
F_x	Axial thrust (N)
F_y	Side force (N)
C_v	Thrust vectoring coefficient
Δ	Deflection angle (degrees)
θ	Flow angle (with respect to nozzle axis)
ν	Prandtl-Meyer angle
C^+, C^-	Characteristics constants
TVC	Thrust vector control
FTV	Fluidic thrust vectoring
SVC	Shock vector control



2D	Two - dimensional
V_x	x - velocity (m/s)
V_y	y - velocity (m/s)
PUV	Primary upstream vortex
SUV	Secondary upstream vortex
SDV	Secondary downstream vortex
PDV	Primary downstream vortex

ACKNOWLEDGMENT

The authors would like to thank the Management of BMS College of Engineering for their support.

REFERENCES

- [1] David J Wing and Victor J Giuliano. Fluidic thrust vectoring of an axisymmetric exhaust nozzle at static conditions. 1997.
- [2] Bruno Mangin, Amer Chpoun, and Laurent Jacquin. Experimental and numerical study of the fluidic thrust vectoring of a two-dimensional supersonic nozzle. In 24th AIAA Applied Aerodynamics Conference, page 3666, 2006.
- [3] Andrew Neely, Fernando Gesto, and John Young. Performance studies of shock vector control fluidic thrust vectoring. In 43rd AIAA/ASME/SAE/ASEE Joint Propulsion Conference & Exhibit, page 5086, 2007.
- [4] Vladeta Zmijanovic, Viviana Lago, Mohamed Sellam, and Amer Chpoun. Thrust shock vector control of an axisymmetric conical supersonic nozzle via secondary transverse gas injection. *Shock Waves*, 24(1):97-111, 2014
- [5] Reginald Williams and Baily Vittal. Fluidic thrust vectoring and throat control exhaust nozzle. In 38th AIAA/ASME/SAE/ASEE Joint Propulsion Conference & Exhibit, page 4060, 2002.
- [6] Karen Deere, Bobby Berrier, Jeffrey Flamm, and Stuart Johnson. Computational study of fluidic thrust vectoring using separation control in a nozzle. In 21st AIAA Applied Aerodynamics Conference, page 3803, 2003
- [7] Karen Deere. Computational investigation of the aerodynamic effects on fluidic thrust vectoring. In 36th AIAA/ASME/SAE/ASEE Joint Propulsion Conference and Exhibit, page 3598, 2000.
- [8] FW Spaid and EE Zukoski. A study of the interaction of gaseous jets from transverse slots with supersonic external flows. *AIAA journal*, 6(2):205-212, 1968.
- [9] Karen Deere. Summary of fluidic thrust vectoring research at nasa langley research center. In 21st AIAA applied aerodynamics conference, page 3800, 2003.
- [10] JH Neilson, A Gilchrist, and CK Lee. Side thrust control by secondary gas injection into rocket nozzles. *Journal of Mechanical Engineering Science*, 10(3):239-251, 1968
- [11] RC Rogers. Model of transverse fuel injection in supersonic combustors. *AIAA Journal*, 18(3):294-301, 1980
- [12] F Forghany, M Taeibe-Rahni, and A Asadollahi-Ghohieh. Numerical investigation of optimization of injection angle effects on fluidic thrust vectoring. *Journal of Applied Fluid Mechanics*, 10(1), 2017.
- [13] M. Ali, Kareem Ahmed, Rajan Kumar, and F. Alvi. Flow field characteristics of oblique shocks generated using microjet arrays. volume 6, 01 2011.
- [14] MJ Zucrow and JD Hoffman. *Gas dynamics*, vol. 1, 2. John Wiley and Sons, New York, 68:69, 1976.
- [15] Maurice Joseph Zucrow and Joe D Hoffman. *Gas dynamics*. volume 2-multidimensional flow. New York, John Wiley and Sons, Inc., 1977. 488 p., 1977
- [16] Michele Ferlauto and Roberto Marsilio. A numerical method for the study of fluidic thrust-vectoring. *Advances in aircraft and spacecraft science*, 3(4):367-378, 2016.
- [17] SHI Jingwei, WANG Zhanxue, ZHOU Li, and SUN Xiaolin. Investigation on flow characteristics of svc nozzles. *Journal of Applied Fluid Mechanics*, 11(2), 2018.
- [18] Venkatesh Gopal, Julian L Klosowiak, Robert Jaeger, Timur Selimkhanov, and Mitra JZ Hartmann. Visualizing the invisible: the construction of three low-cost schlieren imaging systems for the undergraduate laboratory. *European Journal of Physics*, 29(3):607, 2008.